Nonlinear Dyn (2015) 81:169–188
DOI 10.1007/s11071-015-1980-x

ORIGINAL PAPER

A comparison of classical Runge-Kutta and Henon's methods for capturing chaos and chaotic transients in an aeroelastic system with freeplay nonlinearity

Honghua Dai · Xiaokui Yue · Jianping Yuan · Dan Xie · S.N. Atluri

Received: 24 April 2014 / Accepted: 14 February 2015 / Published online: 7 March 2015
© Springer Science+Business Media Dordrecht 2015

Abstract A typical two-dimensional airfoil with freeplay nonlinearity in pitch undergoing subsonic flow is studied via numerical integration methods. Due to the existence of the discontinuous nonlinearity, the classical fourth-order Runge-Kutta (RK4) method cannot capture the aeroelastic response accurately. Particularly, it is because the RK4 method is incapable of detecting the discontinuous points of the freeplay that leads to the numerical instability and inaccuracy. To resolve this problem, the RK4 method is used with the aid of the Henon's method (referred to as the RK4Henon method) to precisely predict the freeplay's switching points. The comparison of the classical RK4 and the RK4Henon methods is carried out in the analyses of periodic motions, chaos, and long-lived chaotic transients. Numerical simulations demonstrate the advantages of the RK4Henon method over the classical RK4 method, especially for the analyses of chaos and chaotic transients. Another existing method to deal with the freeplay nonlinearity is to use an appropriate rational polynomial (RP) to approximate this discontinuous nonlinearity. Consequently, the discontinuity is removed. However, it is demonstrated that the RP approximation method is unable to capture the chaotic transients. In addition, an efficient tool for predicting the existence of chaotic transients is proposed by means of the evolution curve of the largest Lyapunov exponent. Finally, the effects of system parameters on the aeroelastic response are investigated.

Keywords Freeplay nonlinearity · Henon's method · Rational polynomial approximation · Chaotic transient · Largest Lyapunov exponent

H. Dai · X. Yue (✉) · J. Yuan · D. Xie
National Key Laboratory of Aerospace Flight Dynamics, Northwestern Polytechnical University, Xi'an 710072, P.R. China
e-mail: xkyue@nwpu.edu.cn

H. Dai
e-mail: hhdai@nwpu.edu.cn

J. Yuan
e-mail: jyuan@nwpu.edu.cn

D. Xie
e-mail: xiedan2151@163.com.cn

S. N. Atluri
Center for Aerospace Research and Education, University of California, Irvine, California, USA
e-mail: satluri@uci.edu

1 Introduction

Structural nonlinearities may occur in either a distributed or concentrated form. In general, distributed nonlinearity can only become significant when the amplitude of the response is large, while the concentrated nonlinearity may show a significant effect even for vibrations having small amplitude. The freeplay nonlinearity is one of the concentrated nonlinearities and is commonly encountered in mechanical engineering [2,27]. For the present two degrees-of-freedom (DOF) airfoil model, the freeplay nonlinearity has been stud-

ied by several researchers. Yang and Zhao [34] carried out both experimental and theoretical analyses to investigate the limit cycle oscillations (LCOs) of the aeroelastic system, wherein the unsteady aerodynamic force and moment were expressed in terms of the Theodorsen function, and both bilinear and freeplay nonlinearities were studied. Hauenstein and Laurenson [16] conducted an experimental analysis of the airfoil with freeplay nonlinearity, and both LCOs and chaos were observed. Price et al. [28] studied the same model with a freeplay nonlinearity in pitch by the Houbolt's finite difference method in conjunction with the RK4 method. They found that the critical flutter speed for the freeplay nonlinear model was well below the linear flutter speed. Liu et al. [24] proposed an analytical point transformation method to solve the two DOF model with freeplay nonlinearity. Although the point-transformation method can accurately detect the switching points of the freeplay, unfortunately, it is limited to the analysis of periodic motions due to its analytical nature. Abdelkefi et al. [3] investigated the response of the aeroelastic two DOF wing problem both experimentally and theoretically using numerical simulation methods. Vasconcellos et al. [31,32] represented the freeplay nonlinearity by three different representations, namely, discontinuous based on Henon's method, polynomial, and hyperbolic tangent. It was shown that the discontinuous and hyperbolic tangent representations are effective. Additionally, Chung et al. [7] and Liu et al. [22] employed the perturbation-incremental method and the incremental harmonic balance method, respectively, to study the bifurcation of this aeroelastic systems with hysteresis/freeplay nonlinearities. Nevertheless, these analytical methods are limited to the analysis of periodic motions.

In the aforementioned studies, either approximate analytical methods or numerical integration methods were adopted in theoretical analysis. Numerical integration methods, e.g., the RK4, are powerful in solving the nonlinear dynamical problems. In comparison with the approximate analytical methods such as the harmonic balance method [23], the perturbation method [26], and the time domain collocation method [9,11,35], the RK4 is much more straightforward and simpler to use. What is more, the RK4 can be applied to analyze the chaotic responses, while in contrast, the approximate analytical methods cannot work for chaotic analysis due to the periodicity feature of their trial functions. Unfortunately, the RK4 method works well only for systems with distributed nonlinearities. It may fail to produce accurate simulations when a discontinuous nonlinear system is encountered [8,24]. The present system is essentially a combination of three distinct linear subsystems. Hence, it is crucial to accurately detect the switching points between subsystems. Failure to accurately identify the switching points would cause numerical inaccuracy in the analysis of LCOs and even more serious issues in the analysis of chaos.

Henon's method [17] for integrating state-space equations to a prescribed value of a specified state coordinate was applied for the location of the switching points in the freeplay model by Conner et al. [8], Trickey et al. [29]. The method involves integrating the system until a change in linear subdomains occurs. At that moment, the distance the system has traveled into the new subdomain is known. Upon exchanging the dependent variable (the specified variable) and independent variable, viz. time, the ODE system can be integrated back to the exact discontinuous point in merely one step. Conner et al. [8] investigated the effect of the RK4Henon method on the accuracy of calculating periodic motions, by comparing with the RK4 method. It was found that the two methods were consistent with each other in the analysis of LCOs (see also Ref. [1]), except that the two methods may sometimes fall to different LCO attractors for the same set of initial conditions. The present work is a continuation of a previous paper, in which a numerical study of the chaotic motions of a two DOF airfoil with coupled cubic nonlinearities was conducted [10]. Also, as an extension to [8], in this study, the comparison of the RK4 and the RK4Henon methods is carried out, in the analyses of not only LCOs, but also chaos and chaotic transients. The importance of using the RK4Henon method rather than the classical RK4 method will be revealed, when chaotic motions are under consideration. More importantly, we will show that chaotic transients, which can be captured by the RK4Henon method, would be missed out by the RK4 method. The chaotic transients are observed in the present system for the first time.

An alternative strategy to handle the discontinuous nonlinearity is to use a proper rational polynomial (RP) to closely fit the discontinuous function. Alighanbari and Price [5] used a third-order RP function to fit the freeplay nonlinearity, and the resulting continuous system was applied in the analyses of both LCOs and chaos. Liu et al. [22] applied the same strategy

to process the freeplay and hysteresis nonlinearities, and the resulting system was solved by an incremental harmonic balance method; this study was focused on the LCO analysis. Li et al. [21] demonstrated that the RP approximation method is highly accurate in the analysis of LCOs. However, whether the RP approximation method is suitable in the analyses of chaos and chaotic transients has not been answered until now. In this study, the comparison of the RP approximation method and the RK4Henon method will be carried out to answer this question.

Another objective of the present study is to introduce a simple method for predicting the existence of the long-lived chaotic transients. In general, if a very longtime chaotic transient exists before settling into a periodic motion, one would be apt to mistake it as a chaotic motion [15,25]. Vasconcellos et al. [30] showed that this transition phenomenon is probably due to grazing bifurcations. A safe way to avoid this misunderstanding is to run a very long integration time and check the time response to see whether it settles into a periodic motion or not. Here, our method is based on viewing the evolution history of the largest Lyapunov exponent (LLE), that is, a decreasing LLE evolution curve implies the existence of chaotic transient. The present method is simpler and more efficient than the conventional method. Because in the case of chaotic transients, the LLE, if not convergent, will show a decreasing trend sooner than the periodicity begins to emerge in the time response. Finally, the effects of the freeplay nonlinearity, the damping level, and the frequency ratio $\bar{\omega}$ on the aeroelastic response are analyzed by means of bifurcation diagrams.

2 Mathematical model

The mathematical model for the two DOF airfoil in subsonic flow was established by Fung [14]. Although only linear springs in pitch and plunge were considered, the structural nonlinearity can be readily introduced into Fung's formulation. A sketch of the two DOF airfoil with freeplay nonlinearity in pitch is plotted in Fig. 1, in which the positive directions of the pitch angle α and the plunge displacement h are defined.

Including the structural nonlinearity, the linear formulation of Fung [14] is modified into the following non-dimensional form [27]:

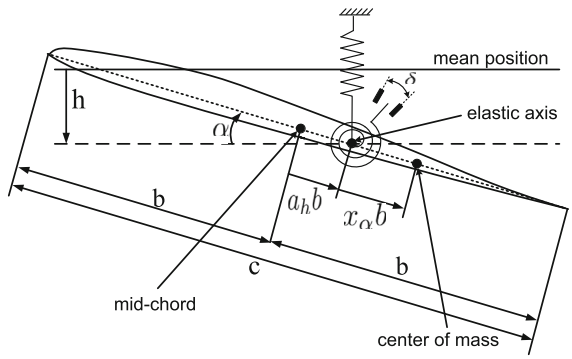

Fig. 1 Sketch of a typical airfoil section with freeplay nonlinearity in pitch

$$\ddot{\xi}+x_\alpha\ddot{\alpha}+2\zeta_\xi\frac{\bar{\omega}}{U^*}\dot{\xi}+\left(\frac{\bar{\omega}}{U^*}\right)^2 G(\xi)=-\frac{1}{\pi\mu}C_L(\tau), \tag{1a}$$

$$\frac{x_\alpha}{r_\alpha^2}\ddot{\xi}+\ddot{\alpha}+2\zeta_\alpha\frac{1}{U^*}\dot{\alpha}+\left(\frac{1}{U^*}\right)^2 M(\alpha)=\frac{2}{\pi\mu r_\alpha^2}C_M(\tau), \tag{1b}$$

where the related symbols are defined in "Appendix 1".

In this study, the plunge spring is linear, and the pitch spring is freeplay nonlinear. Thus, the pitch and plunge stiffness terms $M(\alpha)$ and $G(\xi)$ are expressed as

$$M(\alpha)=\begin{cases} M_0+\alpha-\alpha_f, & \alpha<\alpha_f \\ M_0+M_f(\alpha-\alpha_f), & \alpha_f\le\alpha\le\alpha_f+\delta \\ M_0+\alpha-\alpha_f+\delta(M_f-1), & \alpha>\alpha_f+\delta \end{cases} \tag{2}$$

and $G(\xi)=\xi$, respectively. In fact, the nonlinearity expressed in Eq. (2) is generally referred to as a bilinear nonlinearity, a sketch for which is provided in Fig. 2a. Specifically, the bilinear nonlinearity can be reduced to a freeplay nonlinearity by fixing the stiffness of the freeplay range, viz. M_f, to zero. In most cases, investigators also enforce the preload $M_0=0$ and $\alpha_f=-\frac{1}{2}\delta$, which results in a more special freeplay nonlinearity, as shown in Fig. 2b. In the present study, the general freeplay nonlinearity is analyzed, wherein only $\alpha_f=-\frac{1}{2}\delta$ is fixed for the sake of freeplay symmetry. In numerical simulation, the variations of M_0, M_f and δ will be carried out to show their effects on the aeroelastic response of the present system.

In addition to the structural nonlinearities, $C_L(\tau)$ and $C_M(\tau)$ accounting for linear aerodynamic force and aerodynamic moment are [14]

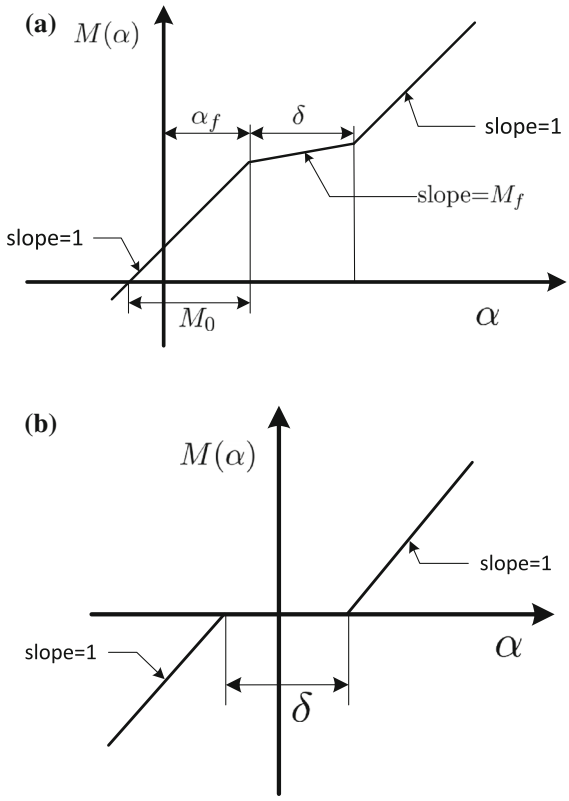

Fig. 2 Sketches of nonlinearity (**a**) bilinear nonlinearity (**b**) simple freeplay nonlinearity

$$
\begin{aligned}
C_L(\tau) = {} & \pi(\ddot{\xi} - a_h\ddot{\alpha} + \dot{\alpha}) \\
& + 2\pi\left[\alpha(0) + \dot{\xi}(0) + \left(\frac{1}{2} - a_h\right)\dot{\alpha}(0)\right]\phi(\tau) \\
& + 2\pi\int_0^\tau \phi(\tau-\sigma)[\dot{\alpha}(\sigma) + \ddot{\xi}(\sigma) \\
& + \left(\frac{1}{2} - a_h\right)\ddot{\alpha}(\sigma)]d\sigma, \qquad (3a)
\end{aligned}
$$

$$
\begin{aligned}
C_M(\tau) = {} & \pi\left(\frac{1}{2} + a_h\right)\left[\alpha(0) + \dot{\xi}(0)\right. \\
& \left. + \left(\frac{1}{2} - a_h\right)\dot{\alpha}(0)\right]\phi(\tau) \\
& + \frac{\pi}{2}(\ddot{\xi} - a_h\ddot{\alpha}) - \frac{\pi}{16}\ddot{\alpha} - \left(\frac{1}{2} - a_h\right)\frac{\pi}{2}\dot{\alpha} \\
& + \pi\left(\frac{1}{2} + a_h\right)\int_0^\tau \phi(\tau-\sigma)\left[\dot{\alpha}(\sigma) + \ddot{\xi}(\sigma)\right. \\
& \left. + \left(\frac{1}{2} - a_h\right)\ddot{\alpha}(\sigma)\right]\mathrm{d}\sigma, \qquad (3b)
\end{aligned}
$$

where the Sears approximation to the Wagner function $\phi(\tau) = 1 - \psi_1 e^{-\epsilon_1\tau} - \psi_2 e^{-\epsilon_2\tau}$ is [6]

$$\phi(\tau) = 1 - 0.165e^{-0.0455\tau} - 0.335e^{-0.3\tau}.$$

System (1) is essentially a set of two integro-differential equations, which cannot be directly integrated. In this study, the original integro-differential equations are transformed into six first-order ODEs with the following two auxiliary variables introduced by Alighanbari and Hashemi [4]:

$$
\begin{aligned}
y_1 = {} & \psi_1 e^{-\epsilon_1\tau}\left[\dot{\xi}(0) + \left(\frac{1}{2} - a_h\right)\dot{\alpha}(0) + \alpha(0)\right] \\
& + \int_0^\tau \psi_1 e^{-\epsilon_1(\tau-\sigma)} \\
& \times\left[\ddot{\xi}(\sigma) + \left(\frac{1}{2} - a_h\right)\ddot{\alpha}(\sigma) + \dot{\alpha}(\sigma)\right]d\sigma, \qquad (4a)
\end{aligned}
$$

$$
\begin{aligned}
y_2 = {} & \psi_2 e^{-\epsilon_2\tau}\left[\dot{\xi}(0) + \left(\frac{1}{2} - a_h\right)\dot{\alpha}(0) + \alpha(0)\right] \\
& + \int_0^\tau \psi_2 e^{-\epsilon_2(\tau-\sigma)} \\
& \times\left[\ddot{\xi}(\sigma) + \left(\frac{1}{2} - a_h\right)\ddot{\alpha}(\sigma) + \dot{\alpha}(\sigma)\right]\mathrm{d}\sigma. \qquad (4b)
\end{aligned}
$$

The integral terms in the aerodynamic force can be suppressed by the introduced two auxiliary variables. Considering Eqs. (4), $C_L(\tau)$ and $C_M(\tau)$ can be rewritten as

$$
\begin{aligned}
C_L(\tau) = \pi\Big[& \ddot{\xi} - a_h\ddot{\alpha} + 2\dot{\xi} + 2\,(1 - a_h)\,\dot{\alpha} \\
& + 2\alpha - 2y_1 - 2y_2\Big],
\end{aligned}
$$

and

$$
\begin{aligned}
C_M(\tau) = \frac{\pi}{2}\Big[& a_h\ddot{\xi} - \left(\frac{1}{8} + a_h^2\right)\ddot{\alpha} + (1 + 2a_h)\dot{\xi} \\
& + a_h(1-2a_h)\dot{\alpha} + (1 + 2a_h)\alpha - (1 + 2a_h)y_1 \\
& - (1 + 2a_h)y_2\Big].
\end{aligned}
$$

Consequently, Eqs. (1) are transformed into a couple of second-order ODEs. In the meanwhile, two additional variables y_1 and y_2 have been introduced into the system. For the system's completeness, two supplemental equations should be constructed. Differentiating Eqs. (4a) and (4b) with respect to τ yields

$$\dot{y}_1 = -\epsilon_1 y_1 + \psi_1\left[\ddot{\xi}(\tau) + (\frac{1}{2} - a_h)\ddot{\alpha}(\tau) + \dot{\alpha}(\tau)\right], \qquad (5a)$$

$$\dot{y}_2 = -\epsilon_2 y_2 + \psi_2\left[\ddot{\xi}(\tau) + (\frac{1}{2} - a_h)\ddot{\alpha}(\tau) + \dot{\alpha}(\tau)\right]. \qquad (5b)$$

Equations (5) are two supplemental first-order ODEs. Therefore, the complete system modeling the typical airfoil section consists of two second-order ODEs, plus two first-order ODEs. Upon introducing $x_1 = \alpha$, $x_2 = \dot{\alpha}$, $x_3 = \xi$, $x_4 = \dot{\xi}$, $x_5 = y_1$ and $x_6 = y_2$, the system can be written in a state-space form as

$$\begin{cases} \dot{x}_1 = x_2, \\ \dot{x}_2 = a_{21}x_1 + a_{22}x_2 + a_{23}x_3 + a_{24}x_4 + a_{25}x_5 \\ \qquad + a_{26}x_6 + m_2 M(x_1), \\ \dot{x}_3 = x_4, \\ \dot{x}_4 = a_{41}x_1 + a_{42}x_2 + a_{43}x_3 + a_{44}x_4 + a_{45}x_5 \\ \qquad + a_{46}x_6 + m_4 M(x_1), \\ \dot{x}_5 = a_{51}x_1 + a_{52}x_2 + a_{53}x_3 + a_{54}x_4 + a_{55}x_5 \\ \qquad + a_{56}x_6 + m_5 M(x_1), \\ \dot{x}_6 = a_{61}x_1 + a_{62}x_2 + a_{63}x_3 + a_{64}x_4 + a_{65}x_5 \\ \qquad + a_{66}x_6 + m_6 M(x_1), \end{cases} \tag{6}$$

where the coefficients are given in "Appendix 2".

In literature, most of the numerical studies have adopted an eight ODE system proposed by Lee's model [18]. The present system (6) consisting of six first-order ODEs is expected to be computationally more efficient than Lee's model. Dai et al. [12] compared the computational efficiency of employing the six ODE model (with cubic nonlinearity) and Lee's model and found that using the six ODE model was approximately 20 % faster. In this study, the six ODE system (6) is applied in all computations.

3 Henon's method

The presence of the discontinuous (or non-smooth) nonlinearity limits the range of application of the classical RK4 method to the analysis of periodic motions, due to the numerical inaccuracy induced by the crossover of the integration step, see Fig. 3.

Linear interpolation method is an intuitive technique to alleviate the numerical inaccuracy. Concretely, one is required to do a linear interpolation between the last two integration points which belong to two neighboring subdomains. Although simple to use, this method may produce an unacceptable error. High-order interpolation methods are available, but suffering from complex programming as well as the storage of a number of previous integration points.

The most effective method for accurately detecting a specified value of a state coordinate (herein x_1) is attributed to Henon [17], wherein Henon's method was

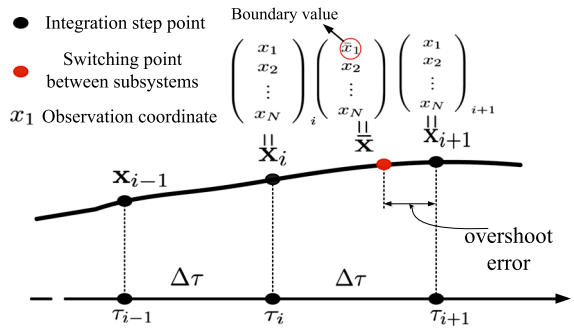

Fig. 3 Error mechanism of the traditional integration method

applied to construct Poincare maps. Henon's method involves integrating the system until a change in linear subdomains is detected. At that time, the distance the system has traveled into the new subdomain is known. By exchanging the dependent variable of interest α and independent variable τ, the system can be integrated from its current location back to the exact point of discontinuity within one step. Then, time is reverted to be the independent variable and the classical RK4 is then applied to integrate the new subsystem in the new subdomain with the initial conditions already known, until a next discontinuity is encountered.

System (6) can be written in state-space form as

$$\frac{d}{d\tau}\begin{pmatrix} x_1 \\ x_2 \\ \vdots \\ x_6 \end{pmatrix} = \begin{pmatrix} f_1(\mathbf{x}) \\ f_2(\mathbf{x}) \\ \vdots \\ f_6(\mathbf{x}) \end{pmatrix}. \tag{7}$$

Henon's method involves exchanging the independent variable τ and the identifying dependent variable x_1, which is accomplished via, first dividing each of the equations in Eqs. (7) by $dx_1/d\tau = f_1(\mathbf{x})$, and then replacing the first equation by $d\tau/dx_1 = 1/f_1(\mathbf{x})$. Consequently, the new system with x_1 being the independent variable is

$$\frac{d}{dx_1}\begin{pmatrix} \tau \\ x_2 \\ \vdots \\ x_6 \end{pmatrix} = \begin{pmatrix} 1/f_1(\mathbf{x}) \\ f_2(\mathbf{x})/f_1(\mathbf{x}) \\ \vdots \\ f_6(\mathbf{x})/f_1(\mathbf{x}) \end{pmatrix}. \tag{8}$$

Note that the new system is used only for one integration step immediately after the identifying variable x_1 crossed the specified value. The RK4Henon method is essentially a variable stepsize integration method, and the stepsize variation happens once the switching point has been crossed.

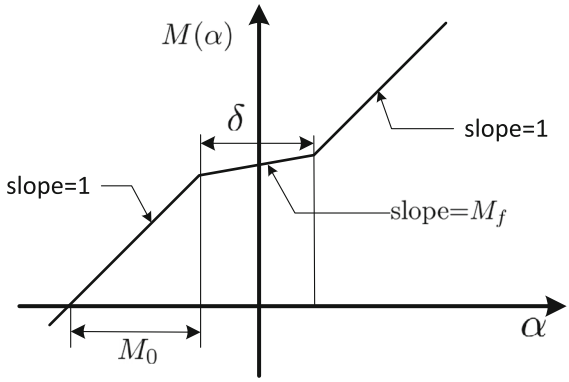

Fig. 4 Sketch of the freeplay nonlinearity with $\alpha_f = -\frac{1}{2}\delta$

Table 1 System parameters for Case 1, 2 and 3

Parameters	Case 1	Case 2	Case 3
a_h	−0.5	−0.5	−0.5
$\bar{\omega}$	0.2	0.2	0.2
μ	100	100	100
x_α	0.25	0.25	0.25
r_α	0.5	0.5	0.5
ζ_α	0	0	0
ζ_ξ	0	0	0
M_0	−0.0025°	0	0
M_f	0.01	0	0
δ	0.5°	0.5°	0.5°
α_f	−0.25°	−0.25°	-0.5δ

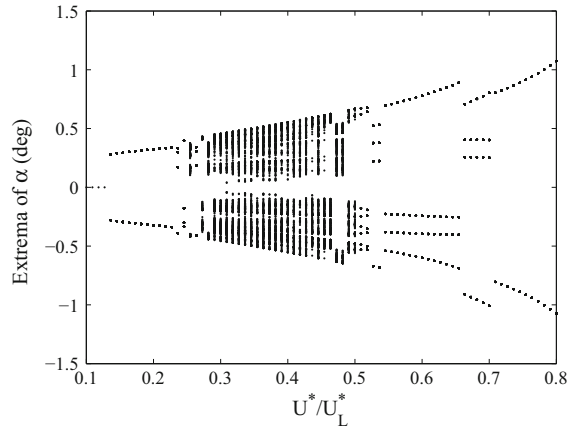

Fig. 5 Bifurcation diagrams for the pitch motion with parameters of Case 1 in Table 1, with initial conditions $\alpha(0) = 3°$ and the rest initial states are zero. The stepsize of the flow speed is $0.01(U^*/U_L^*)$. For each flow speed, the number of integration steps is 2×10^5; the initial 20 % data is dropped off to damp out transients

4 Results and discussions

The sketch of the freeplay nonlinearity considered is plotted in Fig. 4, in which α_f is fixed to be -0.5δ, which means the freeplay range is equally divided by the y axis. In general, the pattern of the freeplay nonlinearity is affected by three factors, namely, the freeplay magnitude δ, the preload M_0, and the pitch stiffness in the freeplay region M_f (in the freeplay range, the stiffness is sometimes not exactly zero). The system parameters are given as Case 1 in Table 1, which are taken from Price et al. [27]. The corresponding linear flutter speed U_L^* is 6.2851.

Figure 5 shows the bifurcation diagram for the pitch motion, which is calculated by the RK4Henon method. It is consistent with the bifurcation diagram calculated by the combination of the finite difference method (FDM) and the classical RK4 method in Price et al. [27], which verifies the consistency of the present six ODE model and the FDM resulting model. However, the coarse comparison by means of the bifurcation diagrams is not sufficient to exhibit the significant difference between the RK4Henon and the classical RK4 methods. Thus, further investigations will be carried out to show the discrepancies between the RK4Henon method and the RK4 method, in the analyses of LCOs, chaos, and chaotic transients.

4.1 Limit cycle oscillations

The RK4 method can produce accurate solutions, provided that LCOs are under consideration [8,24]. Figure 6 shows the comparisons of the time histories and phase portraits by using the RK4Henon and the RK4 at $U^*/U_L^* = 0.6$. This flow speed is selected, according to Fig. 5, to obtain LCOs. Unless otherwise specified, the integration step is $\Delta\tau = 0.1$ throughout the paper. It can be seen that the results by the two methods are in good agreement. However, a partial enlargement in Fig. 6b illustrates that the RK4 phase trajectory contains numerous loops in a limited band, while the RK4Henon trajectory falls exactly in a single loop at current resolution. This indicates that the RK4Henon method is numerically more stable and accurate than the RK4 method. Liu et al. [24] applied both the point transformation method and the RK4 to examine the air-

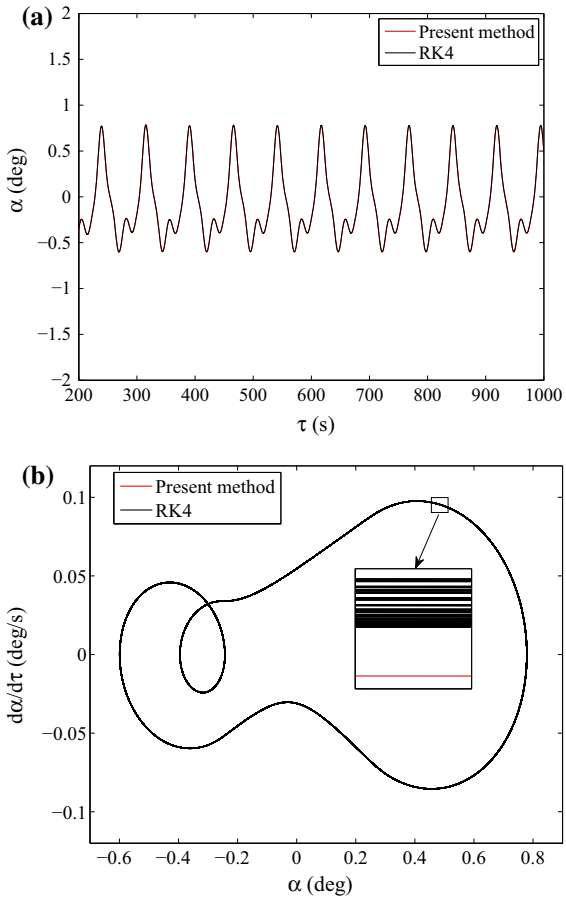

Fig. 6 Comparisons of **a** time histories, and **b** phase plane portraits, for $U^*/U_L^* = 0.6$ using the present RK4Henon method and the RK4 method. The total number of integration steps (For the sake of rigor, we use " the number of integration steps" instead of "integration time" due to the fact that the RK4Henon's stepsize is variable) is 2×10^5.

foil section with freeplay nonlinearity. The numerical results were used as the benchmark solutions to evaluate the results via the point transformation method. However, as stated earlier, the integration time step $\Delta\tau$ has to be very small in order to yield an accurate result. In addition, $\Delta\tau$ can only be selected numerically when the solution computed by $\Delta\tau$ is essentially the same as those obtained using $\Delta\tau/2$ [24], which is a tedious procedure. For the chaotic response, this procedure fails to work.

4.2 Chaotic motions

Having compared the performance of the RK4Henon and the RK4 methods for analyzing LCOs, we turn our attention to their performance in chaotic analysis. Before comparison, we introduce several descriptors of chaos. Normally, time series and phase plane portraits are straightforward hints of chaos. But sometimes, they may not be sufficient to distinguish long-term periodic motions, quasi-periodic motions, and chaos [13].

Table 2 Parameters used during the calculation of LLE

Integration step	0.1 s
Initial conditions, $\alpha(0)$ (and other states being zero)	3°
Time-to-run to eliminate transients	3000 s
Distance between the fiducial and test points[a]	10^{-8}
Number of integrations per rescaling	10
Number of rescalings between printouts	2000
Number of initial LLEs to discard for orientation	20

[a] The initial states of the test particle are specified as $x_{test}(1) = x_{fiducial}(1) + 10^{-8}$ and $x_{test}(i) = x_{fiducial}(i)$, $(i = 2, \ldots, 6)$

The Poincare map is a useful tool to identify chaos. For an autonomous system, its Poincare map is plotted by recording the phase plane points at discrete times when a prescribed "event" occurs. Here, the event is defined as being the passage of a specified coordinate through zero. As suggested by Moon [25], more than 4000 points should be plotted in a Poincare map so as to ensure the integration time is long enough to rule out the possibility of chaotic transients.

A quantitative means to identify chaos is to calculate the largest Lyapunov exponent (LLE) of a time series. A positive LLE indicates that the motion is chaotic, while a nonpositive LLE implies a regular motion. In the present computations, the LLE is calculated based on the algorithms of Wolf et al. [33]. All involved parameters during the calculation of LLE are provided in Table 2. Base-2 instead of base-e is used.

Figure 7 shows the Poincare map, the amplitude spectrum, and the evolution of the LLE for $U^*/U_L^* = 0.27$. As shown in Fig. 7a, the Poincare map is neither a finite set of points (means periodic) nor a closed orbit (means quasi-periodic), which implies that the motion may be chaotic. The amplitude frequency spectrum in Fig. 7b shows a broadband, which is consistent with chaos. To add a further evidence, the LLE has also been calculated. The terminal time for calculating the LLE is different case by case to ensure the convergence of the LLE (if it can converge). As can be seen from Fig. 7c, the LLE converges to approximately 0.009, which indicates mild chaos.

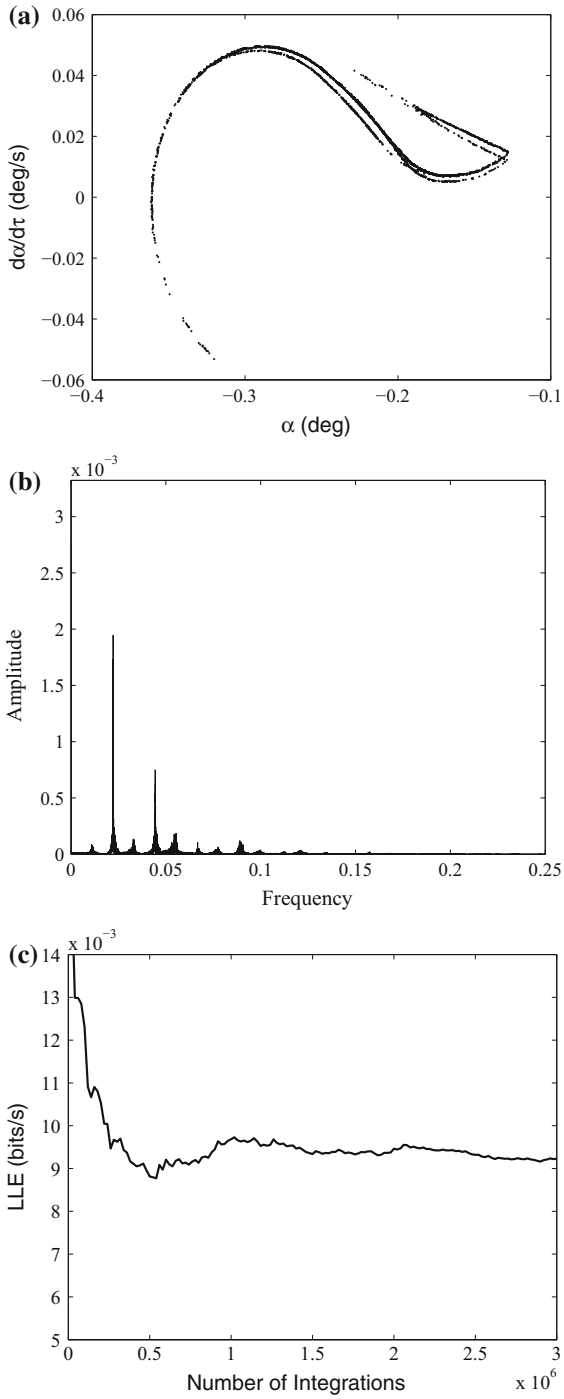

Fig. 7 **a** Poincare map, **b** amplitude spectrum, and **c** evolution history of LLE for $U^*/U_L^* = 0.27$

Shown in Fig. 8 are the time histories for $U^*/U_L^* = 0.27$ by the RK4Henon method and the RK4 method with different integration stepsizes. The time series in Fig. 8 are short segments cut out from long chaotic time series. Although they appear to be rather periodic in this short time range, they are definitely chaotic motions as demonstrated in Fig. 7. It can be seen from Fig. 8 that the RK4 method with a smaller integration step can produce a result closer to the RK4Henon result. Also, it is known that the RK4 with a smaller integration step would generate a more accurate result. That is, the result via RK4 method with $\Delta\tau = 0.001$ is better than that with $\Delta\tau = 0.01$, and similarly result with $\Delta\tau = 0.01$ is better than that with $\Delta\tau = 0.1$. In addition, Fig. 8c shows that RK4 with $\Delta\tau = 0.001$ agrees very well with the RK4Henon. Thus, it can be concluded that the RK4Henon with $\Delta\tau = 0.1$ produces a more accurate result than the RK4 with $\Delta\tau = 0.1$ and RK4 with $\Delta\tau = 0.01$. A further comparison between RK4 with $\Delta\tau = 0.0001$ and the RK4Henon with $\Delta\tau = 0.1$ shows an even closer agreement (not reported in figure), which indicates that the RK4Henon with $\Delta\tau = 0.1$ is better than the RK4 with $\Delta\tau = 0.001$. This demonstrates the accuracy and efficiency of the RK4Henon method over the classical RK4 method. In computations, we also tried the RK4Henon method with $\Delta t = 0.05$ and 0.02 for comparison purpose. We found that deceasing the integration step Δt can increase the accuracy. However, due to the fact that the RK4Henon with $\Delta t = 0.1$ already has a relatively high accuracy, the improvement of using a smaller step is not prominent. Besides, a smaller size step may cause a longer computing time. Therefore, the results of RK4Henon with $\Delta t = 0.05$ and 0.02 are not reported.

It should be emphasized that in the analysis of chaos, even a slight numerical inaccuracy may lead to entirely different solutions after a longtime. Therefore, the RK4Henon method would be the only choice for the chaotic analyses considering (1) its computational economy compared to the classical RK4 method (RK4 requires a much smaller integration stepsize) and (2) its high accuracy (RK4Henon overcomes the numerical instability arising from the crossover during integrations, while RK4 suffers from this).

Shown in Fig. 9 are the time histories and phase portraits computed by RK4Henon with $\Delta\tau = 0.01, 0.1, 0.2, 0.4$. The result by RK4Henon with $\Delta\tau = 0.01$ serves as the benchmark. It can be seen that (1) decreasing the integration step can increase the accuracy of RK4Henon method; (2) $\Delta\tau = 0.1$ is sufficient for

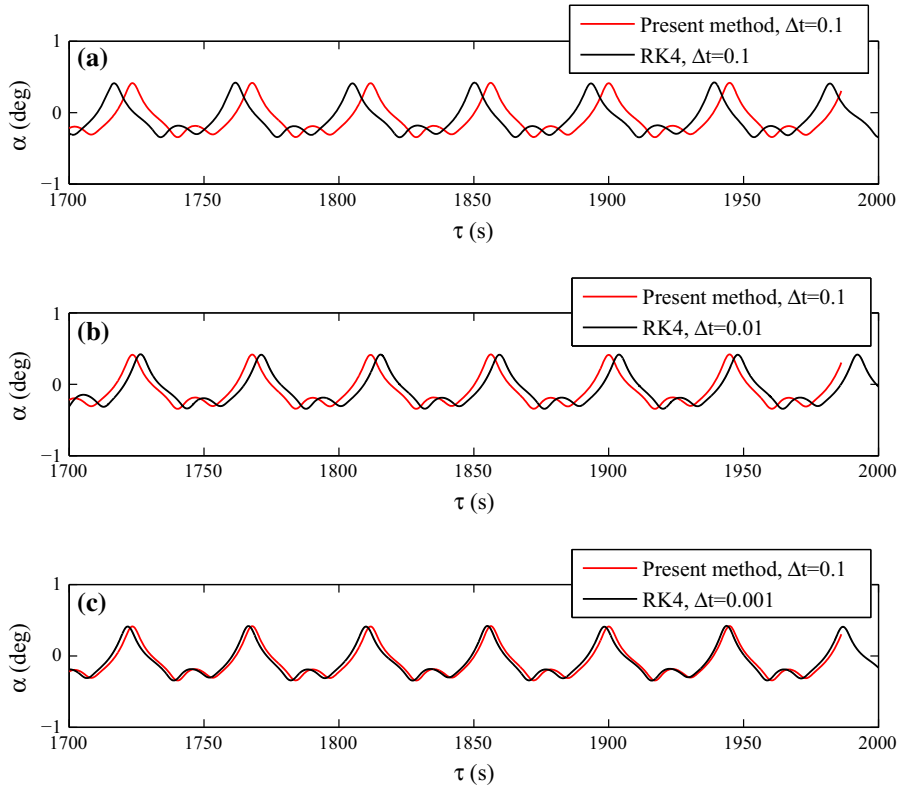

Fig. 8 Comparison of the time series for $U^*/U_L^* = 0.27$ calculated by the RK4Henon, $\Delta\tau = 0.1$ with that calculated by **a** the RK4, $\Delta\tau = 0.1$, **b** the RK4, $\Delta\tau = 0.01$, and **c** the RK4, $\Delta\tau = 0.001$

the present chaotic study; and (3) globally speaking, $\Delta\tau = 0.01,\ 0.1,\ 0.2,\ 0.4$ yield similar results, see Fig. 9b.

In addition, the order of convergence, p, of the RK4Henon method has been evaluated by $p = \log_2 \frac{E_{02\sim04}}{E_{01\sim02}}$, where $E_{02\sim04}$ is the maximum absolute distance of the plunge responses between $\Delta\tau = 0.2$ and 0.4. In the present case, $p \approx 2.1$.

4.3 Chaotic transients

We move our attention to the chaotic transients in this section. Shown in Fig. 10 are the phase portraits, the Poincare maps, and the amplitude spectra for $U^*/U_L^* = 0.3$ by the RK4 and the RK4Henon methods. All three subfigures show that the results by the two methods are qualitatively in very good agreement. In particular, Fig. 10a shows two phase trajectories which spread out the phase plane, implying chaos. Figure 10b shows Poincare maps with many points in a well-organized structure, and Fig. 10c shows two spectra with broadbands. All of these descriptors imply a chaotic motion. However, by careful observation, there seems to be sometime abnormal in Fig. 10b. That is, the structure of the Poincare map by the RK4Henon appears to be much sparser than that by the RK4. Bear in mind that the two methods run the same number of integration steps (2×10^6 integration steps), the RK4Henon's Poincare map should not be so sparse. It implies that a large number of points must be hitting at one or some points, repeatedly.

Now, we turn to the time response curve for help. Figure 11 shows the time histories of the pitch motion for $U^*/U_L^* = 0.3$ by the two methods. We can see that the time series via RK4 corresponds to a chaotic motion, while that via RK4Henon seems to settle to a periodic motion after a longtime (approximately $1.12 \times 10^4 s$) chaotic transient. The phase plane portrait and the Poincare map are replotted in Fig. 12, in which the initial 1.5×10^4 s response has been dropped out before plotting, such that the chaotic transient can be completely damped out. Both the phase trajectory of Fig. 12a and the Poincare map of Fig. 12b show that the response is a period-2 LCO.

Previous studies show that the chaotic transients are difficult to detect. One must always be careful before identifying a random-like motion in a deterministic sys-

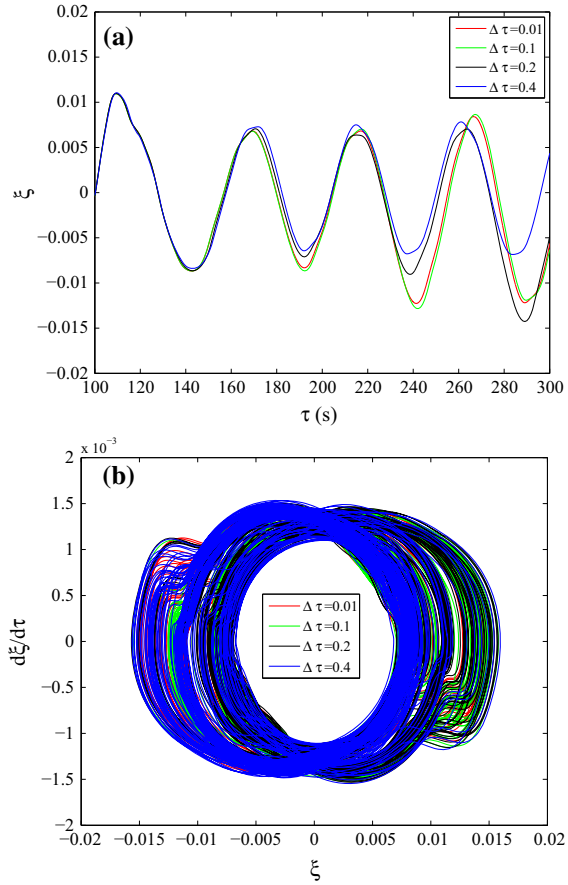

Fig. 9 **a** Time history and **b** phase portrait for $U^*/U_L^* = 0.27$ using RK4Henon with $\Delta\tau = 0.01,\ 0.1,\ 0.2,\ 0.4$

tem to be chaos. Moon [25] suggested that a sufficient longtime must be run before one can safely determine chaos. By his suggestion, the simulation time should be so long such that more than 4000 points have been plotted in the Poincare map. Of course, this time length is not necessary for some short chaotic transients and might be insufficient for some super long-lived chaotic transients. Although simple, this method is not robust and sometimes computationally expensive.

Now, we propose a more robust and economic method for researchers to distinguish chaos and chaotic transients based on the trend of the LLE evolution curve. Figure 13 provides the evolution history of the LLE for the pitch motion calculated by the RK4Henon method for $U^*/U_L^* = 0.3$. It can be seen that the LLE evolution curve has a decreasing trend. In addition, we have already known from Fig. 11c, d that the present motion is a long- term chaotic transient followed by a

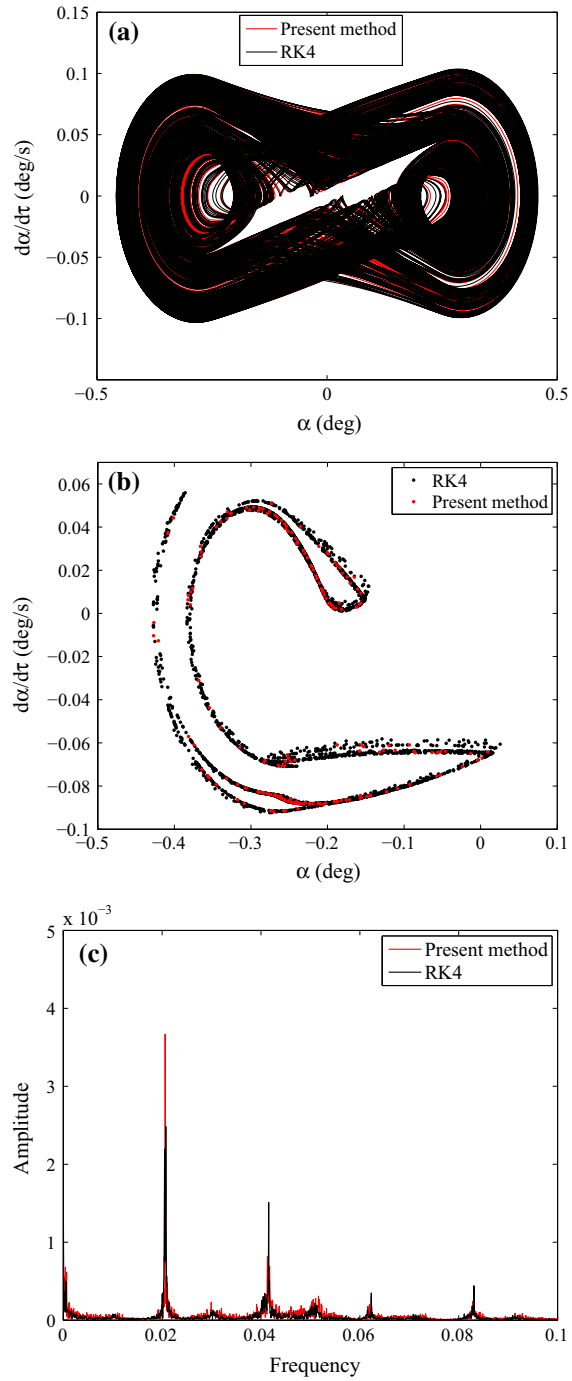

Fig. 10 Comparisons of **a** phase portraits, **b** Poincare maps, and **c** amplitude spectra for $U^*/U_L^* = 0.3$ through using the classical RK4 and the RK4Henon methods

periodic motion. So, it seems that the decreasing LLE evolution curve implies the existence of chaotic transient.

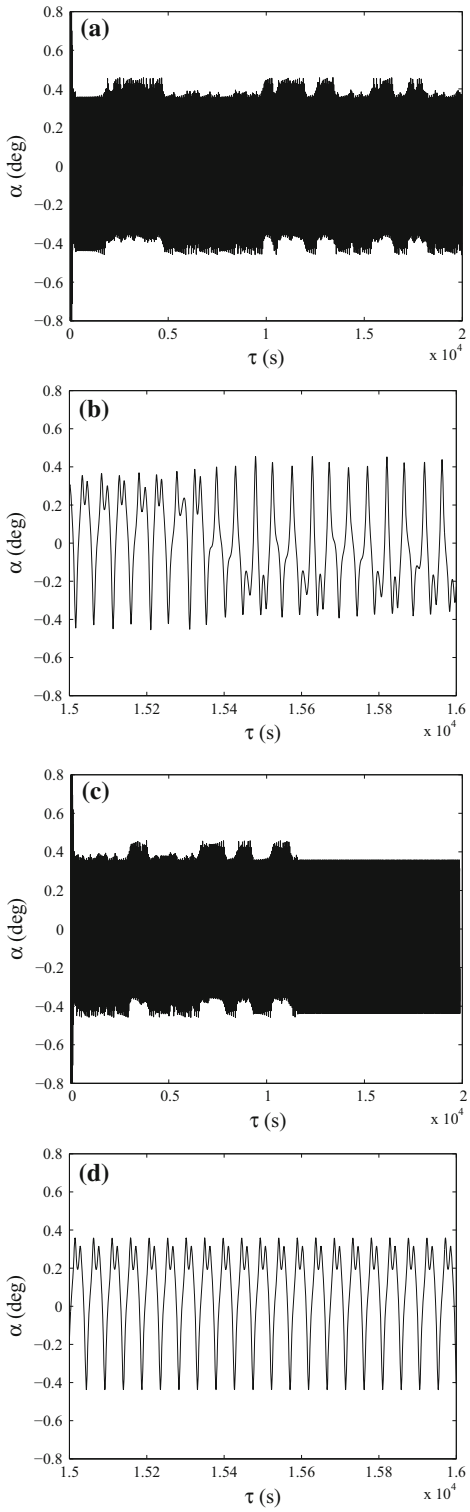

Fig. 11 Time series of the pitch motion for $U^*/U_L^* = 0.3$ via **a** and **b**: the RK4 method, and **c** and **d**: the RK4Henon method. Note that **b** and **d** are cut out from **a** and **c**, respectively

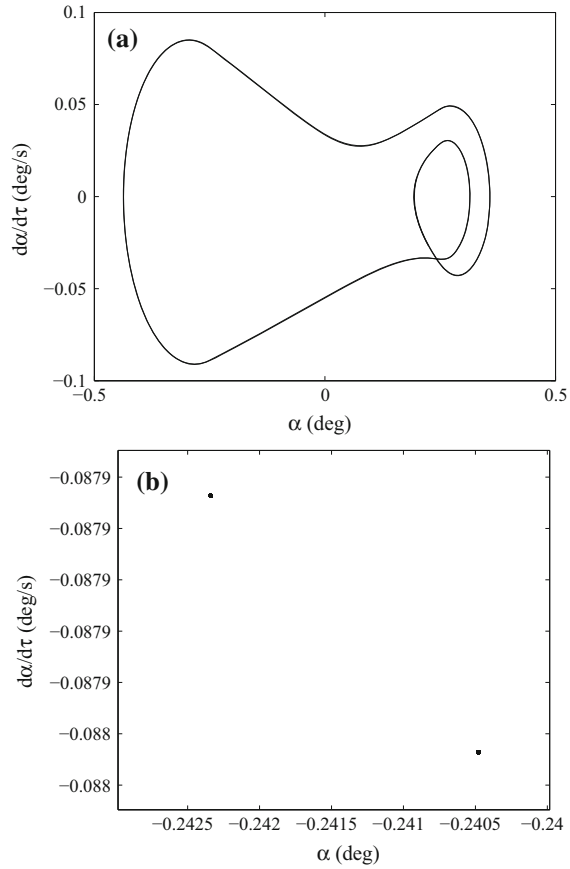

Fig. 12 **a** Phase plane portrait and **b** Poincare map via RK4Henon method after completely damping out transients for $U^*/U_L^* = 0.3$

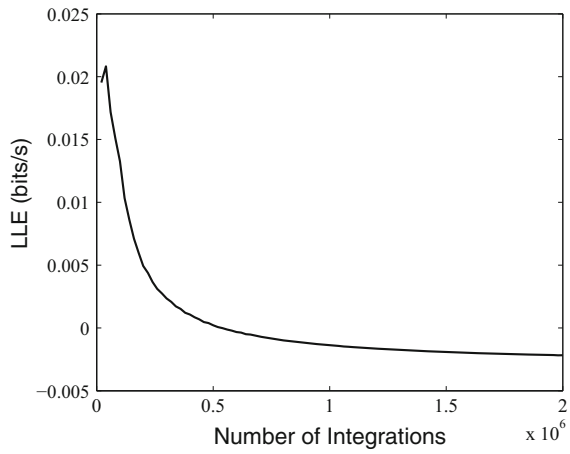

Fig. 13 LLE evolution curves for $U^*/U_L^* = 0.3$ calculated by the RK4Henon method, dropping out the initial 3×10^4 integration steps before calculation

In a previous study [10], the present authors analyzed a two DOF airfoil with a cubic structural nonlinearity. The chaotic transient was detected, and its corresponding LLE evolution curve also showed a decreasing trend. Furthermore, this finding has also been verified in a totally different dynamical system. In an ongoing study, a cantilevered three-dimensional fluttering panel has been analyzed, in which a decreasing LLE evolution curve was also found to be associated with the chaotic transient. Therefore, it is reasonable to conclude that a decreasing LLE evolution curve implies the existence of chaotic transient prior to settling into a periodic motion. This finding provides a simple but efficient tool to determine whether a random-like motion is chaos or chaotic transient.

5 RK4Henon method versus RP approximation method

In this section, we compare the performance of the Rational Polynomial (RP) approximation method and the present RK4Henon method. The RP approximation method consists of first approximating the discontinuous nonlinearity $M(\alpha)$ by a well-fitted rational polynomial and then integrating the resulting continuously dynamical system via the classical RK4. In contrast, the present method directly integrates the original discontinuous system via the highly accurate RK4Henon method. The comparison is carried out in the analyses of LCOs, chaos, and chaotic transients.

5.1 Limit cycle oscillations

The RP approximation is essentially a modification of the dynamical model via smoothing the discontinuous nonlinearity. This technique has been used in many studies, e.g., [5,19,20], however, its validity has not been verified thoroughly. Li et al. [20] applied the RP approximation method to analyze an airfoil with either freeplay or hysteresis nonlinearity. The accuracy of the RP approximation method was proved only in the LCO analysis.

In accordance with [20], we take the system parameters of Case 2 in Table 1. Note that δ in the present study is twice that in [20]. According to Eq. (2), the freeplay nonlinearity is

$$M(\alpha) = \begin{cases} \alpha + 0.25^\circ, & \alpha < 0.25^\circ \\ 0, & 0.25^\circ \le \alpha \le 0.25^\circ \\ \alpha - 0.25^\circ, & \alpha > 0.25^\circ \end{cases} \tag{9}$$

In implementing the RP approximation method, the freeplay nonlinearity is then represented by a rational polynomial using a curve fitting tool in Matlab [20]:

$$M_{RP}(\alpha) = \frac{0.00002747 - 0.01702\alpha - 11.94\alpha^2 + 5462\alpha^3}{0.4556 - 12.36\alpha + 5732\alpha^2}.$$

Figure 14 shows the time histories and the phase portraits for $U^*/U_L^* = 0.35$ by using the RP approximation method and the RK4Henon method. The initial conditions for the numerical simulation are $\alpha = 3^\circ$ and the rest being zero. The phase portraits are plotted after a sufficient longtime has been run to remove transients. Figure 14 indicates that the response is LCO. It can be seen from Fig. 14a, c that the results by the RP approximation are in agreement with those by the RK4Henon in the first 300 seconds. Then, discrepancy occurs between them. The phase portraits in Fig. 14b, d show that the results by the two different methods are different. However, by numerical verification, we confirm that the portraits by the two methods are exactly symmetric about the origin. Thus, the RP approximation method can be used in the analysis of LCOs. This conclusion is consistent with Li et al. [20].

5.2 Chaotic motions

Next, we will show whether the RP approximation method is capable of analyzing the chaotic motions. Figure 15 shows the time histories, phase portraits, Poincare maps, and amplitude spectra for $U^*/U_L^* = 0.26$, where the corresponding response is chaos. It can be seen from the four subfigures that the results by the two different methods are qualitatively in good agreement. However, the inset in Fig. 15a shows that the two results are in excellent agreement in the first 200 seconds, after which the two begin to deviate. The pattern of the phase trajectories in Fig. 15b can ensure that the discrepancy of the time histories in Fig. 15a is not caused by the responses' symmetry, but by the accuracy of the two numerical schemes. Overall, the RP approximation method can be applied in the analysis of chaotic motions to capture the primary feature of chaos.

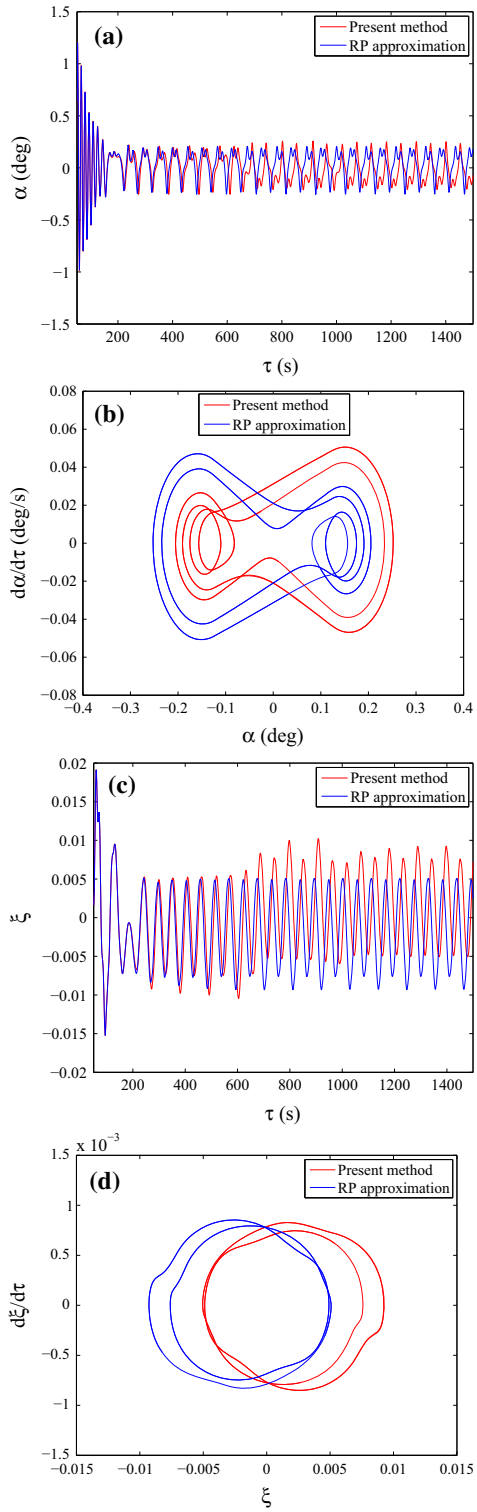

Fig. 14 **a** Time history and **b** phase portrait for pitch motion; **c** time history and **d** phase portrait for plunge motion for $U^*/U_L^* = 0.35$ (LCO)

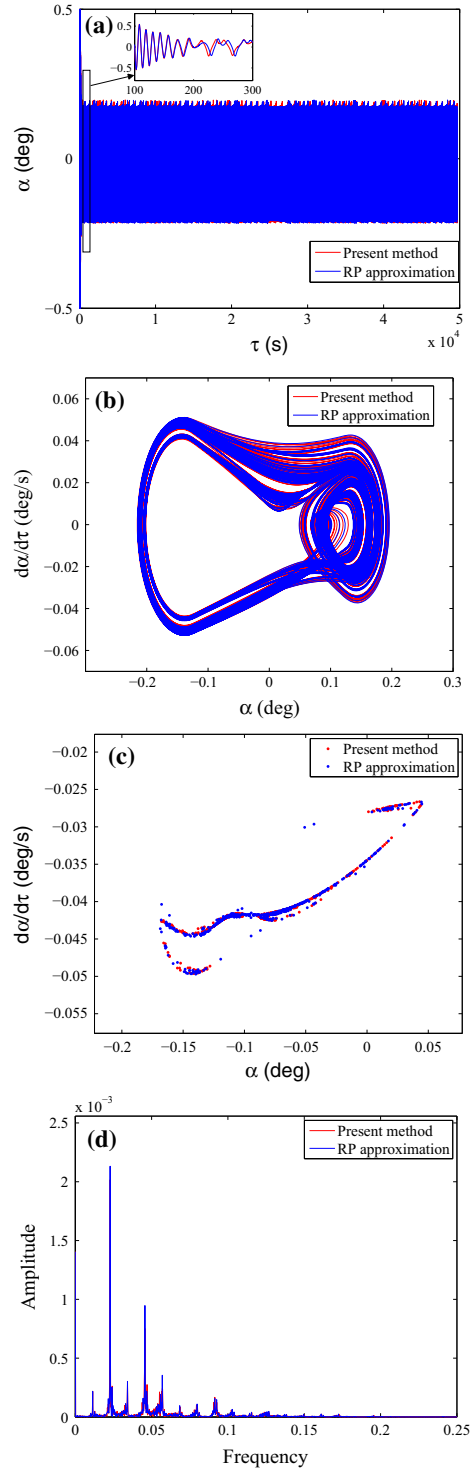

Fig. 15 **a** Time histories, **b** phase portraits, **c** Poincare maps, and **d** amplitude spectra for the pitch motion for $U^*/U_L^* = 0.26$ (chaos) by using the RP approximation method and the RK4Henon method

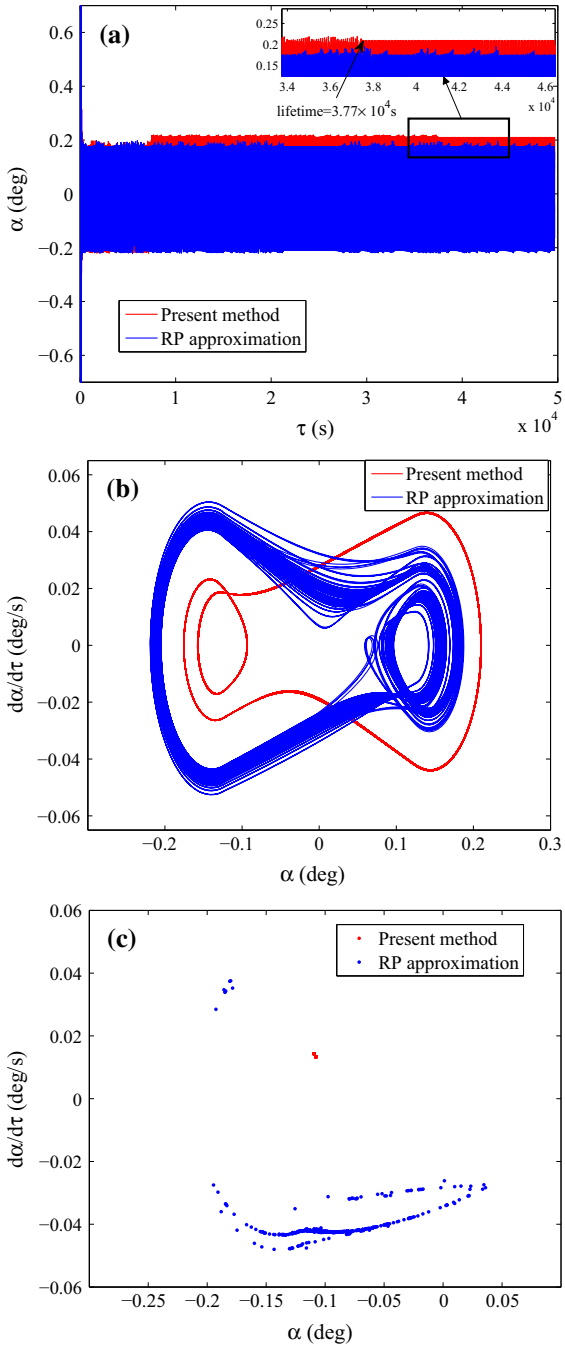

Fig. 16 **a** Time history, **b** phase portrait and **c** Poincare map for the pitch motion for $U^*/U_L^* = 0.27$ (chaotic transient)

5.3 Chaotic transients

Furthermore, the chaotic transients will be analyzed in this part. Shown in Fig. 16 are the time histories, phase portraits, and Poincare maps for $U^*/U_L^* = 0.27$ by the two methods. We can see from Fig. 16a that the two responses agree well until roughly $0.8 \times 10^4\,s$, after which they differ from each other qualitatively. Very interestingly, the inset shows that the time history calculated by the RK4Henon method settles into a periodic motion after a long-lived chaotic transient, while that by the RP approximation method keeps being chaotic. The lifetime of the chaotic transient is up to $3.77 \times 10^4\,s$. Figure 16b, c shows the phase portraits and the Poincare maps, respectively; these figures are constructed after the long-lived chaotic transients have been dropped out. Figure 16b indicates that the response by RK4Henon is indeed periodic (after a very long chaotic transient). Although the two motions are essentially different types, the symmetry of the two trajectories, which was discussed in the LCO case, can be noticed in Fig. 16b. Figure 16c shows the Poincare maps by the two methods. The Poincare map by the RK4Henon contains two adjacent points, which indicates a period-2 motion, while that by the RP approximation method shows a well-organized structure indicating chaos. In sum, the RP approximation method cannot be applied to capture the long-lived chaotic transient followed by a periodic motion.

6 Parametric variations

The effects of the various parameters on the aeroelastic response will be explored in this part. In the following computations, the reference system parameters are provided as Case 3 in Table 1. In the course of investigating a specified parameter, only the one under consideration is varied with the rest being fixed. Except that when δ is varied, the α_f is varied correspondingly. The linear flutter speed U_L^* remains to be 6.2851, and U_L^* keeps unchanged during parametric variations.

6.1 Effect of freeplay nonlinearity

The freeplay nonlinearity is affected by three factors: (1) the freeplay magnitude δ, (2) the preload M_0, and (3) the stiffness in the freeplay range M_f. We will investigate their effect one by one, by means of bifurcation diagrams. In plotting the bifurcation diagrams, the step-size of the flow speed is $0.01(U^*/U_L^*)$.

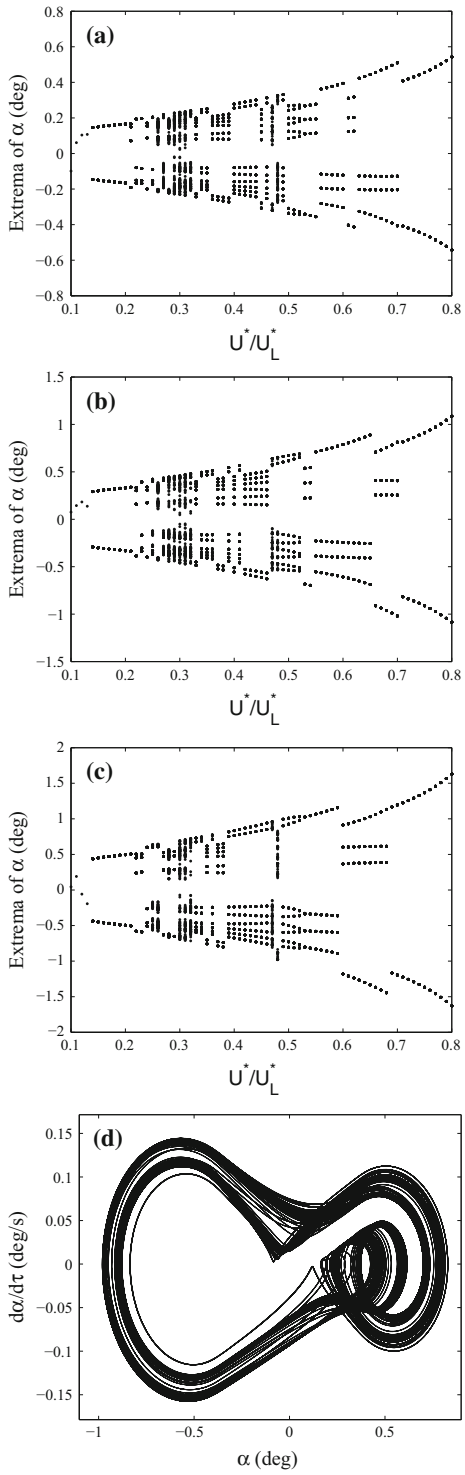

Fig. 17 Bifurcation diagrams plotting α for $\dot{\alpha} = 0$ as a function of U^*/U_L^* for various values of δ: **a** $\delta = 0.25$, **b** $\delta = 0.5$, **c** $\delta = 0.75$; and (**d**), phase portrait for $U^*/U_L^* = 0.48$ for the case with $\delta = 0.75$

6.1.1 Effect of δ

Figure 17 shows the bifurcation diagrams for the pitch motion for various values of freeplay δ. It is seen that as the freeplay δ increases the peak amplitude of the response becomes larger. In particular, the peak amplitudes for $\delta = 0.25,\ 0.5$ and 0.75 are $0.54,\ 1.1$ and 1.6, respectively, for $U^*/U_L^* = 0.8$. On the other hand, the critical flutter speeds for the three cases are almost the same (approximately at $U^*/U_L^* = 0.14$), which means that the magnitude of the freeplay does not alter the critical flutter speed (here, flutter means LCO occurs).

The "flip-over" phenomenon, e.g., around $U^*/U_L^* = 0.6$ in Fig. 17a, is pervasive in bifurcation diagrams. If a parameter marching procedure is employed, "flip-over" can be avoided. Figure 17d shows the phase portrait of the pitch motion for $U^*/U_L^* = 0.48$ in Fig. 17c. Its chaos-like appearance explains the densely plotted vertical line at $U^*/U_L^* = 0.48$ in Fig. 17c. Moreover, we note that the response, prior to the flutter speed, is statically stable with a constant pitch angle. The statically stable response is not the present concern in the present study.

6.1.2 Effect of M_0

Shown in Fig. 18 are the bifurcation diagrams for different values of preload M_0. Overall, the magnitude of the preload does not significantly influence the amplitude of the motions. Specifically, the first two diagrams with $M_0 = -0.0025$ and 0.0025 are similar, except that prior to $U^*/U_L^* = 0.55$, the two responses are symmetric. This symmetric feature can be explained by the solutions' dependance on initial conditions. The comparison between the last two diagrams indicates that increasing the magnitude of the preload may increase the flutter speed.

6.1.3 Effect of M_f

Similarly, the effect of M_f is also investigated. In practice, M_f is much smaller than the linear stiffness, viz. 1. Here, the bifurcation diagrams for $M_f = 0.001,\ 0.02$, and 0.03 are plotted in Fig. 19. Generally speaking, M_f does not significantly influence the response of the aeroelastic system, which can be intuitively understood by the facts that (1) M_f exists only within the freeplay and (2) M_f has a very small value compared with unity.

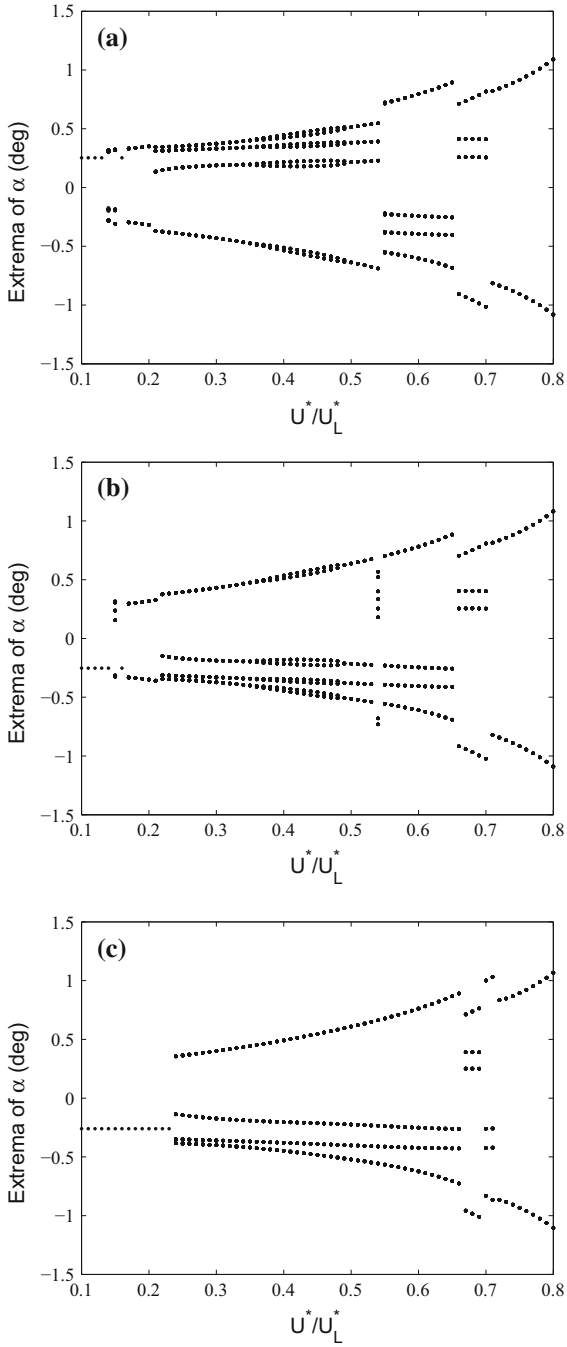

Fig. 18 Bifurcation diagrams plotting α for $\dot{\alpha} = 0$ as a function of U^*/U_L^* for various values of M_0: **a** $M_0 = -0.0025$, **b** $M_0 = 0.0025$, **c** $M_0 = 0.01$

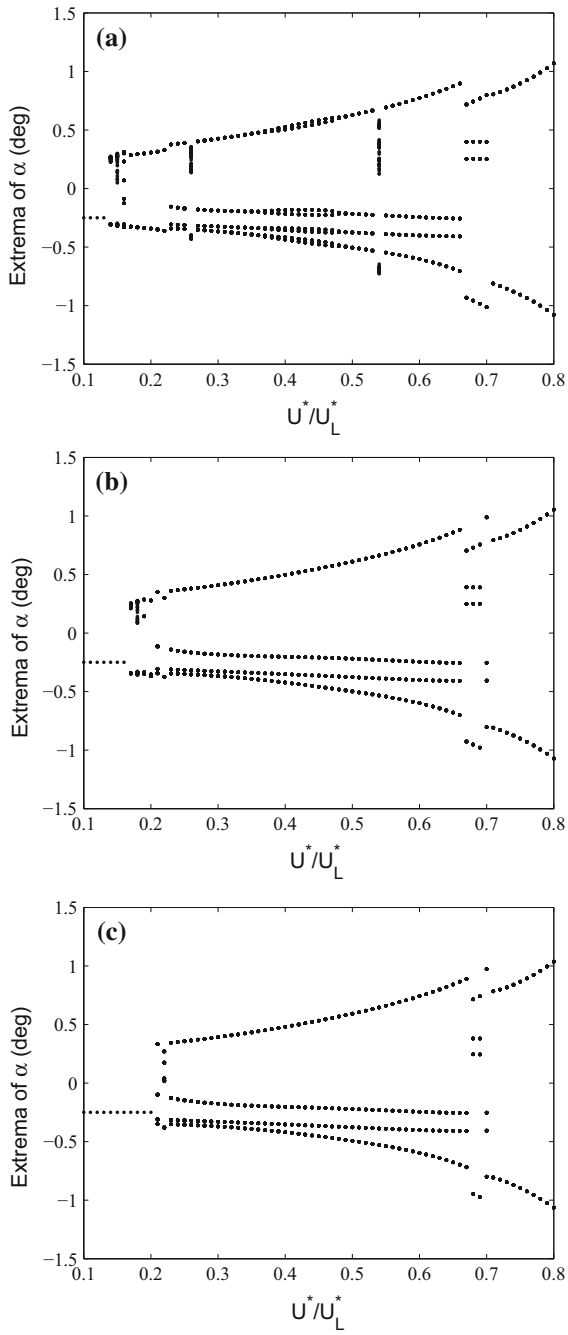

Fig. 19 Bifurcation diagrams plotting α for $\dot{\alpha} = 0$ as a function of U^*/U_L^* for various values of M_f: **a** $M_f = 0.01$, **b** $M_f = 0.02$, **c** $M_f = 0.03$

In detail, we can see from Fig. 19 that a larger value of M_f slightly increases the onset of flutter. In the limiting situation, if the M_f is increased to 1, the present system with freeplay nonlinearity degenerates to a linear system. In this special case, the critical flutter speed is equal to the linear flutter speed U_L^*.

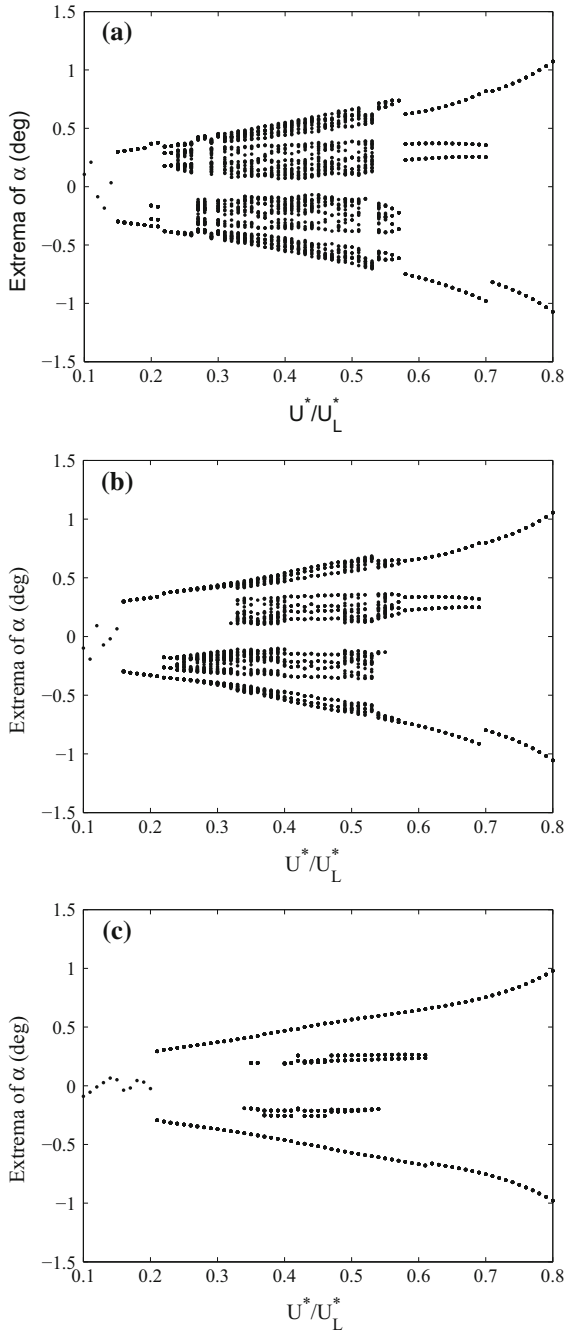

Fig. 20 Bifurcation diagrams plotting α for $\dot{\alpha} = 0$ as a function of U^*/U_L^* for various levels of damping: **a** $\zeta_\alpha = \zeta_\xi = 0.02$, **b** $\zeta_\alpha = \zeta_\xi = 0.04$, **c** $\zeta_\alpha = \zeta_\xi = 0.1$

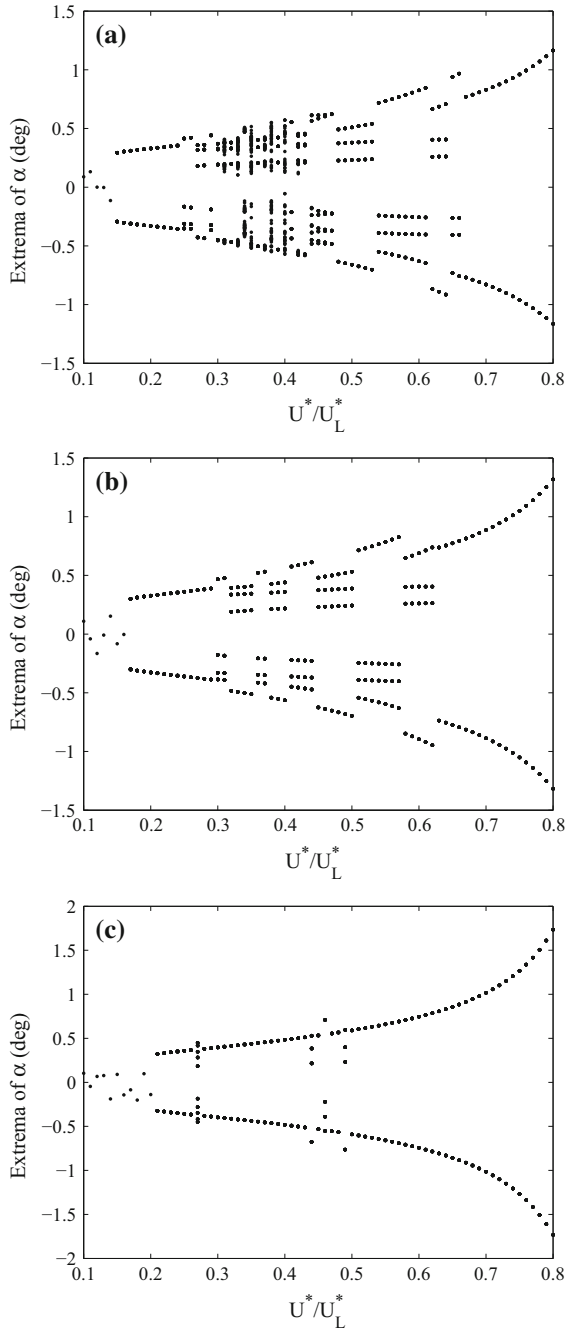

Fig. 21 Bifurcation diagrams plotting α for $\dot{\alpha} = 0$ as a function of U^*/U_L^* for different values of $\bar{\omega}$: **a** $\bar{\omega} = 0.22$, **b** $\bar{\omega} = 0.25$, **c** $\bar{\omega} = 0.3$

6.2 Effect of damping level

Figure 20 provides three bifurcation diagrams for three different levels of damping. As shown in Fig. 20a, when the damping is relatively weak, viz. $\zeta_\alpha = \zeta_\xi = 0.02$, the bifurcation diagram has a chaotic region approximately from 0.25 to 0.57. Increasing the damping to $\zeta_\alpha = \zeta_\xi = 0.04$, the chaotic range will be reduced sig-

nificantly, see Fig. 20b. Further increasing the damping to $\zeta_\alpha = \zeta_\xi = 0.1$, the chaotic response has been completely removed, see Fig. 20c. So, it can be concluded that a reasonably large damping can suppress the presence of chaos, which is consistent with the report of Price et al. [27]. On the other hand, it can be seen by comparing the diagrams in Fig. 20 that the damping can slightly affect the critical flutter speed. Specifically, the critical values for $\zeta_\alpha = \zeta_\xi = 0.02,\ 0.04$ and 0.1 are $U^*/U_L^* = 1.14,\ 1.16$ and 2.11, respectively, which indicates that the damping also has the effect of stabilizing the aeroelastic airfoil. Besides, the damping level does not influence the amplitude of motions.

6.3 Effect of frequency ratio

The bifurcation diagrams for different values of $\bar{\omega}$ are given in Fig. 21. We can see that the response amplitude increases with the increase of $\bar{\omega}$, especially for a relatively large flow speed. For instance, when $U^*/U_L^* = 0.8$, the maximum pitch amplitudes for $\bar{\omega} = 0.22,\ 0.25$ and 0.3 are 1.13, 1.28, and 1.75, respectively. Additionally, the critical flutter speeds for different values of $\bar{\omega}$ are also different. Specifically, flutter speeds for $\bar{\omega} = 0.22,\ 0.25$ and 0.3 are 0.14, 1.16 and 0.21, respectively. It means that increasing the frequency ratio $\bar{\omega}$ can raise the flutter speed of the present two DOF airfoil system. Moreover, it can be seen that the increase in the frequency ratio has an effect of suppressing the occurrence of chaos. Concretely, when $\bar{\omega} = 0.22$, the diagram has a range of chaos. Increasing $\bar{\omega}$ to 0.25, the diagram only exhibits periodic motions. Further increasing $\bar{\omega}$ to 0.3, the diagram shows a much simpler period-1 response.

7 Concluding remarks

A numerical study of the two DOF airfoil with freeplay nonlinearity was carried out. The comparison of the classical RK4 method and the RK4Henon method was conducted in the analyses of LCOs, chaos, and chaotic transients. Some conclusions were drawn. First, the RK4 method can be used to generate a relatively good result in the analysis of LCOs, although there exists an inherent numerical instability due to the crossover of the discontinuous points. Second, the RK4 method cannot capture the chaotic response to a long- term, as in contrast to the RK4Henon method. Even applying a very small integration stepsize, the RK4 method cannot match with the present RK4Henon method. Third and most importantly, the RK4Henon method can capture the long-lived chaotic transient followed by a periodic motion, while the RK4 method cannot. In sum, the RK4Henon method is a better choice when analyzing periodic motions and (perhaps) the only choice for analyzing chaos and chaotic transients. Moreover, the comparison of the RP approximation method and the RK4Henon method has been conducted. It showed that the RP approximation method was suitable for analyzing LCOs, and chaos, but not for chaotic transients.

In addition, a useful tool for identifying chaotic transients, based on viewing the evolution history of the LLE of a time series, was proposed. It was demonstrated that a decreasing LLE history implies the existence of chaotic transient. This finding provides researchers in the dynamics community with an efficient tool to distinguish chaos and long-lived chaotic transients. This method is believed to be more effective than the normally used method, that is, running a very longtime numerical integration to see whether the time history finally settles to a periodic attractor.

Finally, the effects of freeplay, damping level, and frequency ratio on the aeroelastic response were analyzed. For the freeplay nonlinearity, (1) increasing the freeplay magnitude raises the amplitude of the response, but does not change the flutter speed; (2) conversely, increasing the preload of the freeplay nonlinearity increases the flutter speed, but the response amplitude keeps unchanged; and (3) the magnitude of M_f only slightly affects the critical flutter speed. For the effect of damping, we come to two conclusions: (1) increasing the damping level may increase the flutter speed; and (2) the damping has an effect of suppressing the occurrence of chaos. Moreover, the increase in the frequency ratio $\bar{\omega}$ enhances both the response amplitude and the flutter speed.

Acknowledgments This study is financially supported by the Fundamental Research Funds for the Central Universities (3102015ZY008) and the Chinese National Science Foundation (11172235).

Appendix 1: Nomenclature

a_h	Non-dimensional distance from airfoil mid-chord to elastic axis

b	Airfoil semi-chord
$C_L(\tau)$	Coefficient of linear aerodynamic force
$C_M(\tau)$	Coefficient of linear aerodynamic moment
$G(\xi)$	Structural nonlinearity in plunge
h	Plunge deflection
m	Airfoil mass
$M(\alpha)$	Structural nonlinearity in pitch
M_0	Preload of freeplay nonlinearity
M_f	Stiffness in the freeplay range
r_α	Radius of gyration about elastic axis
t	Time
U	Free-stream velocity
U^*	$U/b\omega_\alpha$, non-dimensional velocity
U_L^*	Non-dimensional linear flutter speed
x_α	Non-dimensional distance from airfoil elastic axis to center of mass
α	Pitch angle
α_f	Parameter in freeplay nonlinerity
δ	Magnitude of freeplay
$\epsilon_1,\ \epsilon_2$	Constants in Wagner's function
ϕ	Wagner's function
μ	$m/\pi\rho b^2$
ρ	Air density
τ	Ut/b, non-dimensional time
ω	Fundamental circular frequency of the motion
$\omega_\xi,\ \omega_\alpha$	Natural frequencies in plunge and pitch
$\bar{\omega}$	ω_ξ/ω_α, frequency ratio
ξ	h/b, non-dimensional plunge deflection
$\psi_1,\ \psi_2$	Constants in Wagner's function
$\zeta_\alpha,\ \zeta_\xi$	Viscous damping ratios in pitch and plunge
$\dot{(\ )}$	$d(\ )/d\tau$

Appendix 2: Coefficients in system (6)

$$
\begin{aligned}
a_{21} &= f_0(d_0c_4 - c_0d_4)\\
a_{22} &= f_0(d_0c_3 - c_0d_3)\\
a_{23} &= f_0d_0c_7\\
a_{24} &= f_0(d_0c_2 - c_0d_2)\\
a_{25} &= f_0(d_0c_5 - c_0d_5)\\
a_{26} &= f_0(d_0c_6 - c_0d_6)\\
m_2 &= -f_0c_0d_7\\
a_{41} &= -f_0(d_1c_4 - c_1d_4)\\
a_{42} &= -f_0(d_1c_3 - c_1d_3)\\
a_{43} &= -f_0d_1c_7\\
a_{44} &= -f_0(d_1c_2 - c_1d_2)\\
a_{45} &= -f_0(d_1c_5 - c_1d_5)\\
a_{46} &= -f_0(d_1c_6 - c_1d_6)\\
m_4 &= f_0c_1d_7\\
a_{51} &= [f_0(c_1d_4 - d_1c_4) + f_0f_1(d_0c_4 - c_0d_4)]\,\psi_1\\
a_{52} &= [f_0(c_1d_3 - d_1c_3) + f_0f_1(d_0c_3 - c_0d_3) + 1]\,\psi_1\\
a_{53} &= \psi_1 f_0(f_1d_0c_7 - d_1c_7)\\
a_{54} &= [f_0(c_1d_2 - d_1c_2) + f_0f_1(d_0c_2 - c_0d_2)]\,\psi_1\\
a_{55} &= -\epsilon_1 + [f_0(c_1d_5 - d_1c_5) + f_0f_1(d_0c_5 - c_0d_5)]\,\psi_1\\
a_{56} &= [f_0(c_1d_6 - d_1c_6) + f_0f_1(d_0c_6 - c_0d_6)]\,\psi_1\\
m_5 &= \psi_1 f_0(c_1d_7 - f_1c_0d_7)\\
a_{61} &= [f_0(c_1d_4 - d_1c_4) + f_0f_1(d_0c_4 - c_0d_4)]\,\psi_2\\
a_{62} &= [f_0(c_1d_3 - d_1c_3) + f_0f_1(d_0c_3 - c_0d_3) + 1]\,\psi_2\\
a_{63} &= \psi_2 f_0(f_1d_0c_7 - d_1c_7)\\
a_{64} &= [f_0(c_1d_2 - d_1c_2) + f_0f_1(d_0c_2 - c_0d_2)]\,\psi_2\\
a_{65} &= [f_0(c_1d_5 - d_1c_5) + f_0f_1(d_0c_5 - c_0d_5)]\,\psi_2\\
a_{66} &= -\epsilon_2 + [f_0(c_1d_6 - d_1c_6) + f_0f_1(d_0c_6 - c_0d_6)]\,\psi_2\\
m_6 &= \psi_2 f_0(c_1d_7 - f_1c_0d_7)
\end{aligned}
$$

where

$$
\begin{aligned}
&c_0 = 1 + \frac{1}{\mu} \quad d_0 = \frac{x_\alpha\mu - a_h}{\mu r_\alpha^2} \quad f_0 = \frac{1}{c_0d_1 - c_1d_0}\\
&c_1 = x_\alpha - \frac{a_h}{\mu} \quad d_1 = 1 + \frac{1 + 8a_h^2}{8\mu r_\alpha^2} \quad f_1 = \frac{1}{2} - a_h\\
&c_2 = 2\left(\zeta_\xi\frac{\bar{\omega}}{U^*} + \frac{1}{\mu}\right) \quad d_2 = -\frac{1 + 2a_h}{\mu r_\alpha^2}\\
&c_3 = \frac{2(1 - a_h)}{\mu} \quad d_3 = 2\frac{\zeta_\alpha}{U^*} - \frac{a_h(1 - 2a_h)}{\mu r_\alpha^2}\\
&c_4 = \frac{2}{\mu} \quad d_4 = -\frac{1 + 2a_h}{\mu r_\alpha^2}\\
&c_5 = c_6 = -c_4 \quad d_5 = d_6 = -d_4\\
&c_7 = \left(\frac{\bar{\omega}}{U^*}\right)^2 \quad d_7 = \left(\frac{1}{U^*}\right)^2
\end{aligned}
$$

References

1. Abdelkefi, A., Nayfeh, A.H., Hajj, M.R.: Modeling and analysis of piezoaeroelastic energy harvesters. Nonlinear Dyn. **67**(2), 925–939 (2012)
2. Abdelkefi, A., Vasconcellos, R., Marques, F.D., Hajj, M.R.: Bifurcation analysis of an aeroelastic system with concentrated nonlinearities. Nonlinear Dyn. **69**(1–2), 57–70 (2012)
3. Abdelkefi, A., Vasconcellos, R., Nayfeh, A.H., Hajj, M.R.: An analytical and experimental investigation into limit-cycle oscillations of an aeroelastic system. Nonlinear Dyn. **71**(1–2), 159–173 (2013)
4. Alighanbari, H., Hashemi, S.M.: Derivation of ODEs and bifurcation analysis of a two DOF airfoil subjected to

unsteady incompressible flow. Int. J. Aerosp. Eng. **2009**, 1–7 (2009)
5. Alighanbari, H., Price, S.J.: The post-hopf-bifurcation response of an airfoil in incompressible two-dimensional flow. Nonlinear Dyn. **10**(4), 381–400 (1996)
6. Bisplinghoff, R.L., Ashley, H.: Aeroelasticity. Courier Dover Publications, New York (1996)
7. Chung, K.W., Chan, C.L., Lee, B.H.K.: Bifurcation analysis of a two-degree-of-freedom aeroelastic system with freeplay structural nonlinearity by a perturbation-incremental method. J. Sound Vib. **299**(3), 520–539 (2007)
8. Conner, M.D., Virgin, L.N., Dowell, E.H.: Accurate numerical integration of state-space models for aeroelastic systems with free play. AIAA J. **34**(10), 2202–2205 (1996)
9. Dai, H.H., Schnoor, M., Atluri, S.N.: A simple collocation scheme for obtaining the periodic solutions of the duffing equation, and its equivalence to the high dimensional harmonic balance method: subharmonic oscillations. Comput. Model. Eng. Sci. **84**(5), 459–497 (2012)
10. Dai, H.H., Yue, X.K., Xie, D., Atluri, S.N.: Chaos and chaotic transients in an aeroelastic system. J. Sound Vib. **333**(26), 7267–7285 (2014)
11. Dai, H.H., Yue, X.K., Yuan, J.P.: A time domain collocation method for obtaining the third superharmonic solutions to the duffing oscillator. Nonlinear Dyn. **73**(1–2), 593–609 (2013)
12. Dai, H.H., Yue, X.K., Yuan, J.P., Atluri, S.N.: A time domain collocation method for studying the aeroelasticity of a two dimensional airfoil with a structural nonlinearity. J. Comput. Phys. **270**, 214–237 (2014)
13. Dowell, E.H.: Observation and evolution of chaos for an autonomous system. J. Appl. Mech. **51**(3), 664–673 (1984)
14. Fung, Y.C.: An introduction to the theory of aeroelasticity. Wiley, New York (1955)
15. Grebogi, C., Ott, E., Yorke, J.A.: Super persistent chaotic transients. Ergod. Theory Dyn. Syst **5**, 341–372 (1985)
16. Hauenstein, A.J., Laurenson, R.M.: Chaotic response of aerosurfaces with structural nonlinearities. Tech. rep., DTIC Document (1989)
17. Henon, M.: On the numerical computation of poincaré maps. Phys. D **5**(2), 412–414 (1982)
18. Lee, B.H.K., Gong, L., Wong, Y.S.: Analysis and computation of nonlinear dynamic response of a two-degree-of-freedom system and its application in aeroelasticity. J. Fluids Struct. **11**(3), 225–246 (1997)
19. Lee, B.H.K., Price, S.J., Wong, Y.S.: Nonlinear aeroelastic analysis of airfoils: bifurcation and chaos. Prog. Aerosp. Sci. **35**(3), 205–334 (1999)
20. Li, D.C., Guo, S.J., Xiang, J.W.: Aeroelastic dynamic response and control of an airfoil section with control surface nonlinearities. J. Sound Vib. **329**(22), 4756–4771 (2010)
21. Li, D.C., Xiang, J.W., J, G.S.: Study of the conditions that cause chaotic motion in a two-dimensional airfoil with structural nonlinearities in subsonic flow. J. Fluids Struct. **33**, 109–126 (2012)
22. Liu, J.K., Chen, F.X., Chen, Y.M.: Bifurcation analysis of aeroelastic systems with hysteresis by incremental harmonic balance method. Appl. Math. Comput. **219**(5), 2398–2411 (2012)
23. Liu, L., Dowell, E.H.: The secondary bifurcation of an aeroelastic airfoil motion: effect of high harmonics. Nonlinear Dyn. **37**(1), 31–49 (2004)
24. Liu, L., Wong, Y.S., Lee, B.H.K.: Non-linear aeroelastic analysis using the point transformation method, part 1: Freeplay model. J. Sound Vib. **253**(2), 447–469 (2002)
25. Moon, F.C.: Chaotic vibrations: an introduction for applied scientists and engineers. Wiley, New York (1987)
26. Nayfeh, A.H., Mook, D.T.: Nonlinear oscillations. Wiley, New York (1979)
27. Price, S.J., Alighanbari, H., Lee, B.H.K.: The aeroelastic response of a two-dimensional airfoil with bilinear and cubic structural nonlinearities. J. Fluids Struct. **9**(2), 175–193 (1995)
28. Price, S.J., Lee, B.H.K., Alighanbari, H.: Poststability behavior of a two-dimensional airfoil with a structural nonlinearity. J. Aircr. **31**(6), 1395–1401 (1994)
29. Trickey, S.T., Virgin, L.N., Dowell, E.H.: The stability of limit-cycle oscillations in a nonlinear aeroelastic system. Proc. R. Soc. Lond. Ser A Math. Phys. Eng. Sci. **458**(2025), 2203–2226 (2002)
30. Vasconcellos, R., Abdelkefi, A., Hajj, M.R., Marques, F.D.: Grazing bifurcation in aeroelastic systems with freeplay nonlinearity. Commun. Nonlinear Sci. Numer. Simul. **19**(5), 1611–1625 (2014)
31. Vasconcellos, R., Abdelkefi, A., Marques, F., Hajj, M.R.: Control surface freeplay nonlinearity: Modeling and experimental validation. In: 53rd AIAA/ASME/ASCE/AHS/ASC Structures, Structural Dynamics and Materials Conference 20th AIAA/ASME/AHS Adaptive Structures Conference 14th AIAA (2012)
32. Vasconcellos, R., Abdelkefi, A., Marques, F.D., Hajj, M.R.: Representation and analysis of control surface freeplay nonlinearity. J. Fluids Struct. **31**, 79–91 (2012)
33. Wolf, A., Swift, J.B., Swinney, H.L., Vastano, J.A.: Determining lyapunov exponents from a time series. Phys. D **16**(3), 285–317 (1985)
34. Yang, Z.C., Zhao, L.C.: Analysis of limit cycle flutter of an airfoil in incompressible flow. J. Sound Vib. **123**(1), 1–13 (1988)
35. Yue, X.K., Dai, H.H., Liu, C.S.: Optimal scale polynomial interpolation technique for obtaining periodic solutions to the duffing oscillator. Nonlinear Dyn. **77**, 1455–1468 (2014)